

A full general relativistic neutrino radiation-hydrodynamics simulation of a collapsing very massive star and the formation of a black hole

Takami Kuroda,^{1★} Kei Kotake,² Tomoya Takiwaki³ and Friedrich-Karl Thielemann^{4,5}

¹*Institut für Kernphysik, Technische Universität Darmstadt, Schlossgartenstrasse 9, D-64289 Darmstadt, Germany*

²*Department of Applied Physics, Fukuoka University, 8-19-1, Jonan, Nanakuma, Fukuoka, 814-0180, Japan*

³*Division of Theoretical Astronomy, National Astronomical Observatory of Japan (NAOJ), 2-21-1, Osawa, Mitaka, Tokyo, 181-8588, Japan*

⁴*Department of Physics, University of Basel, Klingelbergstrasse 82, CH-4056 Basel, Switzerland*

⁵*GSI Helmholtzzentrum für Schwerionenforschung, Planckstrasse 1, D-64291 Darmstadt, Germany*

Accepted XXX. Received YYY; in original form ZZZ

ABSTRACT

We study the final fate of a very massive star by performing full general relativistic (GR), three-dimensional (3D) simulation with three-flavor multi-energy neutrino transport. Utilizing a 70 solar mass zero metallicity progenitor, we self-consistently follow the radiation-hydrodynamics from the onset of gravitational core-collapse until the second collapse of the proto-neutron star (PNS), leading to black hole (BH) formation. Our results show that the BH formation occurs at a post-bounce time of $T_{\text{pb}} \sim 300$ ms for the $70 M_{\odot}$ star. This is significantly earlier than those in the literature where lower mass progenitors were employed. At a few ~ 10 ms before BH formation, we find that the stalled bounce shock is revived by intense neutrino heating from the very hot PNS, which is aided by violent convection behind the shock. In the context of 3D-GR core-collapse modeling with multi-energy neutrino transport, our numerical results present the first evidence to validate a *fallback* BH formation scenario of the $70 M_{\odot}$ star.

Key words: supernovae: general — stars: black holes — hydrodynamics — neutrinos

1 INTRODUCTION

It is now of great importance to unveil the origin of “massive” black holes after the first gravitational-wave (GW) detection by the LIGO collaboration (Abbott et al. 2016a). Since then, a rich variety of the BH masses (~ 8 to $35 M_{\odot}$) have been discovered in binary black hole (BBH) merger events (e.g., Abbott et al. 2016b, 2017).

One of the most plausible scenarios to explain the BBHs is a binary stellar evolution in a low-metallicity environment (see Abbott et al. (2016c) for a review). It has been proposed that two massive stars in the approximate range of 40 to $100 M_{\odot}$ lead to the formation of a massive helium core (e.g., Belczynski et al. (2010); Langer (2012); Kinugawa et al. (2016) for collective references therein). The gravitational collapse of the massive core ($\sim 30 M_{\odot}$) could account for some of the relevant BH mass ranges (at least in the high-mass end) in the GW events, although the formation path to the massive core and further on to the BH is still very uncertain due to the complexity of the binary evo-

lution and the fallback dynamics (e.g., Fryer et al. (1999); Heger et al. (2003); Belczynski et al. (2014)).

In order to clarify the formation process of the BH, one requires full general relativistic and neutrino radiation-hydrodynamics core-collapse simulations of such massive stars in three-dimensional space. Due to the high numerical cost (e.g., Janka et al. (2016); Lentz et al. (2015); Kotake et al. (2012)), most of the previous studies with BH formation have been performed assuming spherical symmetry (1D) (e.g., Liebendörfer et al. (2004); Sumiyoshi et al. (2007); Fischer et al. (2009); O’Connor & Ott (2011)). In multi-dimensional (multi-D) simulations, Sekiguchi & Shibata (2005), Ott et al. (2011), and Cerdá-Durán et al. (2013) were among the first to study the BH formation of very rapidly rotating stars in GR but with simplified microphysics setups (e.g., polytropic equation of state (EOS) and/or a neutrino leakage scheme). In the context of multi-D simulations with multi-energy neutrino transport, Chan et al. (2018) were the first to report a BH-forming 3D-GR simulation of a 40 solar mass zero-metallicity star. They reported that the shock revival occurs at 0.35 s after bounce which is ~ 0.2 s before the

★ E-mail: takami.kuroda@physik.tu-darmstadt.de

BH formation. More recently, [Pan et al. \(2017\)](#) reported a similar result from post-Newtonian simulations of a 40 solar mass solar metallicity star, using a two-flavor IDSA scheme ([Liebendörfer et al. 2009](#)) and a leakage scheme for the heavy-flavor neutrinos. [Ott et al. \(2018\)](#) performed a series of 3D-GR simulations of solar-metallicity stars with multi-energy neutrino transport. Their most massive progenitor ($40 M_{\odot}$) leads to the most energetic explosion among the computed models, where the BH formation was not followed due to the shorter simulation timescale ($T_{\text{pb}} \sim 300$ ms postbounce). Comparing their 1D (non-exploding) $40 M_{\odot}$ model, note that the BH formation would occur later than $T_{\text{pb}} \sim 600 - 700$ ms. Thus far the BH formation has not yet been explored in the context of 3D simulations with two-moment neutrino transport schemes in GR as proposed in [Shibata et al. \(2011\)](#); [Cardall et al. \(2013\)](#).

In this Letter, we study the final fate of a 70 solar mass zero metallicity star by performing 3D-GR core-collapse simulation with the best available neutrino transport scheme ([Kuroda et al. 2016](#)). Our results show that the BH formation time ($T_{\text{pb}} \sim 300$ ms) is significantly shorter than those obtained in the previous multi-D simulations ($T_{\text{pb}} \sim 1$ s) where the $40M_{\odot}$ stars have only been investigated so far ([Chan et al. 2018](#); [Pan et al. 2017](#)). Our results present the first numerical evidence to extend the horizon of the validity of the fallback scenario up to a $70M_{\odot}$ star where the neutrino-driven shock revival precedes the BH formation.

2 NUMERICAL METHODS AND INITIAL MODEL

The numerical schemes in this work are essentially the same as those in [Kuroda et al. \(2016\)](#). Regarding the metric evolution, we evolve the standard BSSN variables ([Shibata & Nakamura 1995](#); [Baumgarte & Shapiro 1999](#); [Marronetti et al. 2008](#)) with a finite-difference scheme in space and with a Runge-Kutta method in time, both in fourth-order accuracy. The gauge is specified by the “1+log” lapse and by the Gamma-driver-shift condition. Regarding the radiation-hydrodynamic evolution, the conservation equation $\nabla_{\alpha} T_{(\text{total})}^{\alpha\beta} = 0$ is solved using the piecewise parabolic method ([Colella & Woodward 1984](#); [Hawke et al. 2005](#)). $T_{(\text{total})}^{\alpha\beta}$ is the total stress-energy tensor,

$$T_{(\text{total})}^{\alpha\beta} = T_{(\text{fluid})}^{\alpha\beta} + \int d\varepsilon \sum_{\nu \in \nu_e, \bar{\nu}_e, \nu_x} T_{(\nu, \varepsilon)}^{\alpha\beta}, \quad (1)$$

where $T_{(\text{fluid})}^{\alpha\beta}$ and $T_{(\nu, \varepsilon)}^{\alpha\beta}$ are the stress-energy tensor of the fluid and the neutrino radiation field, respectively. We consider three-flavor of neutrinos ($\nu \in \nu_e, \bar{\nu}_e, \nu_x$) with ν_x denoting heavy-lepton neutrinos (i.e., ν_{μ}, ν_{τ} and their anti-particles). ε represents the neutrino energy measured in the comoving frame which logarithmically covers from 1 to 300 MeV with 12 energy bins. Employing an M1 analytical closure scheme ([Shibata et al. 2011](#)), we solve spectral neutrino transport of the radiation energy and momentum, based on the truncated moment formalism (e.g., [Kuroda et al. \(2016\)](#); [Roberts et al. \(2016\)](#); [Ott et al. \(2018\)](#)). We include the gravitational red- and Doppler-shift terms to follow the neutrino radiation field in highly curved spacetime around BH. Regarding neutrino opacities, the standard weak interaction

set in [Bruenn \(1985\)](#) plus nucleon-nucleon Bremsstrahlung ([Hannestad & Raffelt 1998](#)) is taken into account.

We use a 70 solar mass zero-metallicity star of [Takahashi et al. \(2014\)](#), which we refer to as Z70 below. At the precollapse phase of Z70, the mass of the central iron core is $\sim 2.8M_{\odot}$ and the enclosed mass up to the helium layer is $\sim 31M_{\odot}$. By comparing with an ultra metal-poor star with a similar progenitor mass (a $75M_{\odot}$ star of [Woosley et al. \(2002\)](#), hereafter referred to as U75), the two progenitors are rather similar especially in the vicinity of the central cores, such as the progenitor’s core-compact parameter ([O’Connor & Ott 2011](#)) ($\xi_{2.5} \sim 1.00$ and 0.86 for Z70 and U75, respectively), the central density and temperature (albeit being slightly higher ($\sim 10\%$) for Z70). We thus consider that our results would not change significantly even if we use U75. For comparing with previous results, we also compute a 40 solar mass solar metallicity star of [Woosley et al. \(2002\)](#) that we refer to as S40. Note that the compactness parameter of S40 is much smaller ($\xi_{2.5} \sim 0.26$) than that of Z70.

We use the equation of state (EOS) by [Lattimer & Swesty \(1991\)](#) with a bulk incompressibility modulus of $K = 220$ MeV (LS220). The 3D computational domain is a cubic box with 15,000 km width, and nested boxes with nine refinement levels are embedded in the Cartesian coordinates. Each box contains 64^3 cells and the minimum grid size near the origin is $\Delta x = 458$ m. The PNS core surface (~ 10 km) and stalled shock (~ 110 - 220 km) are resolved by $\Delta x = 458$ m and 7.3 km, respectively.

3 RESULTS

The top panel of Fig.1 shows the time evolution of the maximum (rest-mass) density ρ_{max} (solid lines) and the minimum lapse α_{min} (dotted lines) for Z70 (red line) and S40 (black line), respectively. The maximum density at bounce ($\rho_{\text{max}} \sim 4 \times 10^{14} \text{ g cm}^{-3}$) is quite similar for the two models. After bounce, one can see that the increase of the maximum density of Z70 (red solid line) is significantly faster than that of S40 (black solid line). In Z70, we stop the computation at $T_{\text{fin}} = 293$ ms after bounce because it exceeds the (temperature) range of the EOS table used in our simulation. In both Z70 and S40, the minimum lapse (dotted lines) shows a gradual decrease after bounce. At around T_{fin} , it shows a drastic drop to $\alpha_{\text{min}} = 0.0645$ for Z70.

In the bottom panel of Fig.1, we explain how T_{fin} is related to the BH formation time. We show the profiles of (angle-averaged) density (black lines) and a diagnostics to measure the BH formation as a function of the enclosed baryon mass M_b at some representative snapshots near T_{fin} for Z70 (red lines) and at $T_{\text{pb}} = 400$ ms for S40 (green line). We estimate the diagnostics by the ratio r_s/R where r_s and R are the Schwarzschild radius and the radial coordinate, respectively. One can see that the maximum r_s/R is ~ 0.3 at 2.359 ms before T_{fin} (the thin red line labelled by “-2.359 [ms]”) and rapidly increases with time, approaching to unity (precisely, 0.9932) at T_{fin} (thickest red line), which we judge as the epoch of the BH formation in this work. For the unambiguous definition of the BH formation, one requires the implementation of the so-called apparent horizon finder (e.g., [Thornburg \(2004\)](#)) in numerical relativity simulation, which we leave for future work.

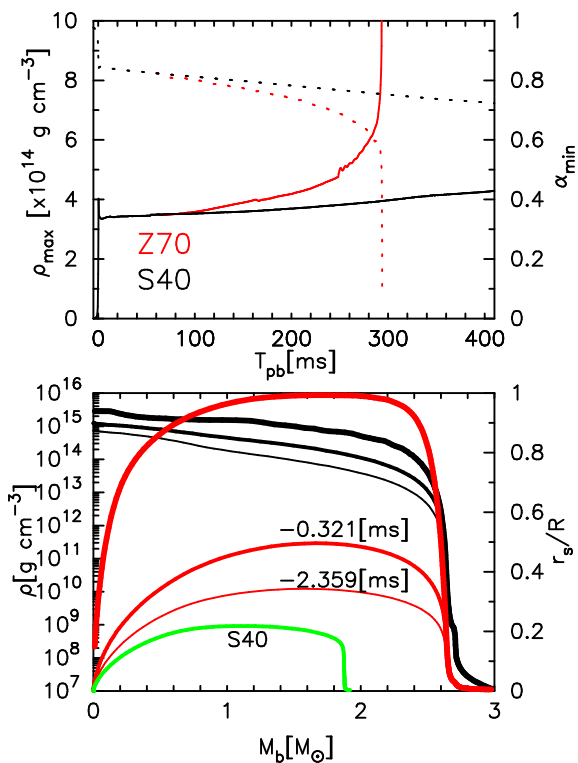


Figure 1. *Top:* Time evolution of the maximum rest mass density (solid line) and minimum lapse function (dotted line) for Z70 (red line) and S40 (black line), respectively. *Bottom:* Spatial profiles of the rest mass density (black line) and the ratio r_s/R (red lines, see text) for Z70 as a function of the enclosed baryon mass for three representative time slices near the final simulation time. “-0.321” and “-2.359” ms denote the time before the final simulation time ($T_{\text{fin}} = 293$ ms after bounce). The green line corresponds to r_s/R for S40 at $T_{\text{pb}} = 400$ ms.

At the (fiducial) BH formation time, the mass and the radius are $M_{\text{b(g),BH}} \sim 2.60(2.51) M_\odot$ and $R_{\text{iso}} \sim 4$ km, respectively (see the thickest red line in the bottom panel of Fig.1). By contrast, S40 shows a significantly less compact structure (green line) at the final simulation time ($T_{\text{pb}} = 400$ ms). The BH formation should occur much later, possibly when the mass shell at $R(M_b = 2.6M_\odot) \sim 10^9$ cm accretes onto the stalled shock. Using the same EOS (LS220), this expectation is in line with Chan et al. (2018) who reported the BH formation at $T_{\text{pb}} \sim 1$ s.

Fig. 2 displays the time evolution of the (angle-averaged) shock radius R_s , the gain radius R_g , the diagnostic explosion energy E_{exp} (see Eq.(2) of Müller et al. (2012)), the ratio of the advection timescale to the neutrino-heating timescale in the gain region $\tau_{\text{adv}}/\tau_{\text{heat}}$ (e.g., Buras et al. (2006); Kuroda et al. (2012)), and the mass in the gain region M_{gain} , respectively. For Z70 (red solid lines), one can clearly see the shock revival after $T_{\text{pb}} \gtrsim 260$ ms and rapid increase in E_{exp} . E_{exp} finally reaches $\sim 1.2 \times 10^{50}$ erg which is, however, two orders of magnitude smaller than the binding energy ahead of the shock. In this second collapse phase, the high neutrino emission makes the heating timescale shorter than the competing advection timescale in the gain region. Aided by strong convection behind the shock, the stalled shock is revived at $T_{\text{pb}} \gtrsim 260$ ms ($\tau_{\text{adv}}/\tau_{\text{heat}} \geq 1$, red line in

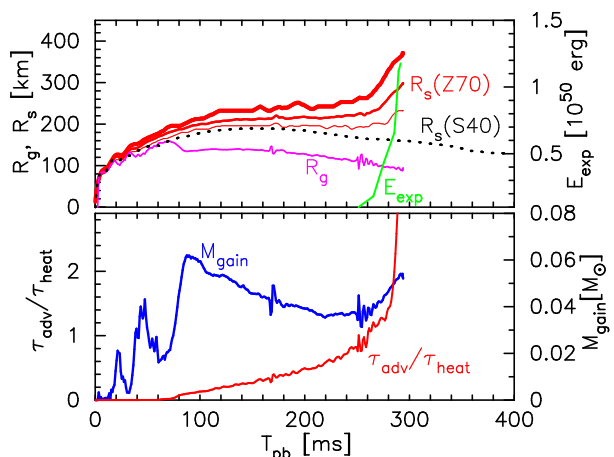


Figure 2. *Top:* Postbounce evolution of the (angle-averaged) shock radii R_s (red, black), the gain radius R_g (magenta), and diagnostic explosion energy E_{exp} (green). The red lines correspond to the maximum, average, and minimum radii for Z70 and the black dotted line is (only) the average radius for S40. *Bottom:* The ratio of the advection timescale to the neutrino heating timescale in the gain region $\tau_{\text{adv}}/\tau_{\text{heat}}$ (red line) and the mass in the gain region M_{gain} (blue line) for Z70.

the bottom panel of Fig.2). This also results in the increase in the gain mass (see the blue line) due to the shock expansion. We note that the shock stall radii $R \sim 200(180)$ km in Z70(S40) are rather larger than previous reports, e.g., ~ 160 km for S40 in Ott et al. (2018). We consider that this comes most likely from a low numerical resolution of $\Delta X = 7.3$ km around the shock surface (approximately two or more times coarser than that employed in Ott et al. (2018)), which could seed stronger prompt convection.

Fig.3 visualizes the hydrodynamic evolution in 3D after the shock stall (panel (a)), through the onset of convection (panels (b) and (c)), toward the shock-revival and the BH formation (panel (d)). During the first ~ 160 ms after bounce, the neutrino heating is still weak and the high entropy bubbles do not appear (panel (a)). After $T_{\text{pb}} \gtrsim 230$ ms, high entropy plumes with $s \gtrsim 15k_B$ baryon $^{-1}$ are visible (panel (b)). At this time, the mass in the gain region M_{gain} also starts to increase (Fig. 2). Comparing panel (c) with (d), the expansion of the (merging) high entropy plumes is clearly seen, leading to the shock revival. The lapse function shows the steepest drop in the center (panel (d), see the cusp in the yellowish plane), which corresponds to the BH formation. By expanding the shock radius in spherical harmonics, we find that the deviation of the shock from spherical symmetry (in the low-modes $\ell = 1, 2$) is less than $\sim 2\%$. This clearly indicates that neutrino-driven convection dominates over the SASI (standing accretion shock instability, Blondin et al. (2003)) in this case.

Finally, we show in Fig. 4 the gravitational waveform for the cross mode and the spectrogram of wave strain with assuming a source distance of $D = 10$ kpc (top), the neutrino luminosity (middle), and rms neutrino energy (bottom) for Z70. The waveform is extracted along the positive z -axis via a standard quadrupole formula (Kuroda et al. 2014) where the GR corrections are taken into account (e.g., Shibata & Sekiguchi (2003)). The rms neutrino energies and

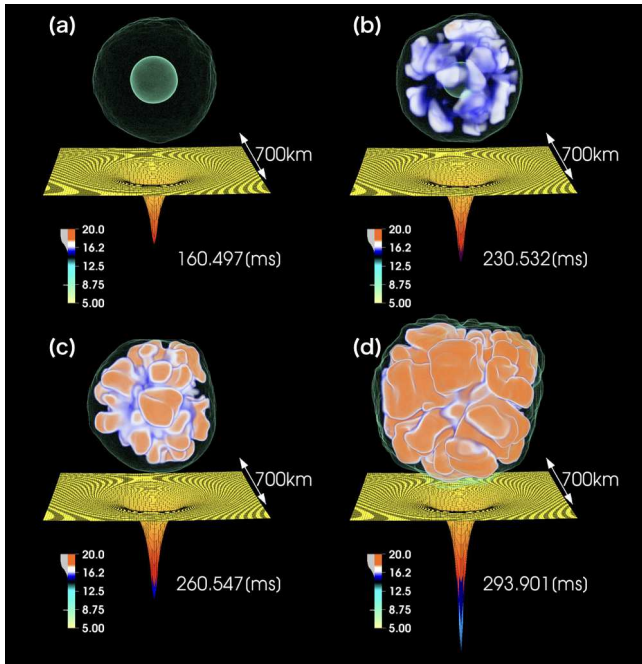


Figure 3. Snapshots of the entropy distribution (k_B baryon $^{-1}$) for Z70 at $T_{\text{pb}} \sim 160, 231, 261,$ and 294 ms (from *top left to bottom right*), respectively. The sheet represents the lapse function (α) on the $z = 0$ plane.

neutrino luminosities are obtained from the radiation energy and flux in the comoving frame at $R_{\text{iso}} = 400$ km, respectively.

The GW amplitude stays at a small value $Dh \lesssim 10$ cm before the shock expansion occurs. The strong GW emission most likely originates from the g -mode oscillation of the PNS and strong convection motion behind the shock (e.g., panels (c) and (d) in Fig.3). This can be understood from broad band emissions $100 \lesssim F \lesssim 3000$ Hz in the spectrogram. Such a broad-band feature is consistent with Ott et al. (2011) who showed the GW amplitudes reaching $Dh \sim 30$ cm for their non-rotating model. Note that there are significant differences between our numerical method and the ones in Ott et al. (2011) who assumed octant symmetry with different numerical resolution than ours, used polytropic EOS, and omitted neutrino radiation.

The neutrino luminosity and rms energy of electron type (anti-)neutrinos show a decreasing and plateau trend for $T_{\text{pb}} \gtrsim 260$ ms, respectively. On the other hand, heavy-lepton neutrinos show a rapid increase both in the luminosity and rms energy¹. As previously identified in 1D full-GR simulations with Boltzmann neutrino transport (Liebendörfer et al. 2004), these features are commonly observed in the literature, due to rapid contraction of the

¹ We find a transient increment at $T_{\text{pb}} \sim 40$ ms in $\langle E_{\nu_x} \rangle_{\text{rms}}$. We consider that this might be due to stronger shock and prompt convection motions which upscatter neutrinos. Since this transient increment diminishes for the mean energy $\langle E_{\nu_x} \rangle_{\text{mean}}$, only a small portion of neutrinos are affected. It could be the artifact of mesh refinement boundary and/or relatively low numerical resolution. Simulation with large number of grids is necessary to clarify this issue.

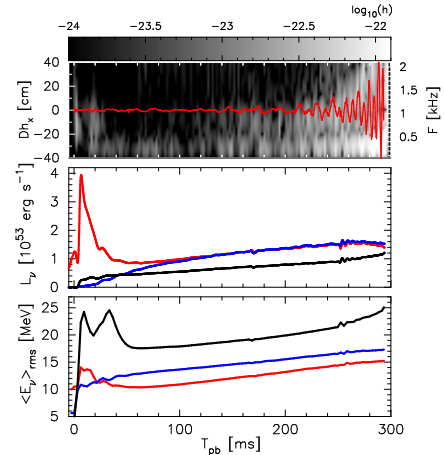


Figure 4. Gravitational waveform and its spectrogram (top), Neutrino luminosities (middle), and rms neutrino energies (bottom) as a function of post-bounce time for Z70. Note in the top panel that h_x and D denotes the GW amplitude of the cross polarization and the distance to the source, respectively. Red, blue, and black lines represent ν_e , $\bar{\nu}_e$, and ν_x , respectively.

PNS to the forming BH (see also, Sumiyoshi et al. (2007); Fischer et al. (2009); Hempel et al. (2012)). The detection of the short-live (~ 300 ms after bounce) neutrino signals are basically limited to Galactic events (see Mirizzi et al. (2016) for a review). However, further study would be needed to clarify the contribution of these BH forming massive stars to the prediction of the diffuse supernova neutrino background (e.g., Lunardini (2009); Horiuchi et al. (2018)).

4 SUMMARY AND DISCUSSIONS

We have presented the results of full 3D-GR core-collapse simulations of massive stars with three-flavor spectral neutrino transport using the M1 closure scheme. Employing a 70 solar mass zero metallicity progenitor, we self-consistently followed the 3D hydrodynamics from the onset of gravitational core-collapse until the second collapse of the PNS, leading to the BH formation. We showed that the BH formation occurs at the post-bounce time of $T_{\text{pb}} \sim 300$ ms for the $70 M_{\odot}$ star, which is significantly earlier than found in the literature. At a few ~ 10 ms before the BH formation, the neutrino-driven shock revival was obtained, which is aided by violent convection behind the shock. Although it requires much longer simulation time to evaluate the final explosion energy E_{exp} and also determine if the mass ejection occurs, E_{exp} , at the BH formation time, is significantly lower than the binding energy ahead of the shock. This indicates that the mass ejection would be hardly expected. Our full 3D-GR core-collapse simulations, however, present the first evidence to validate the BH formation by fallback (Heger et al. 2003) up to the $70 M_{\odot}$ star, where the neutrino-driven shock revival precedes the BH formation. We also presented analysis on the neutrino emission which possesses characteristic signatures of the second collapse.

Note that this is the first simulation where the $70 M_{\odot}$ of Takahashi et al. (2014) was employed. We shortly compare our results with previous works that focused on the

BH formation. O'Connor & Ott (2011) studied in their extensive 1D simulations the impact of progenitors and EOSs on the BH formation while simplifying neutrino physics by a leakage scheme. Their U75 model using the same EOS (LS220) shows $M_{\text{b(g),BH}} \sim 2.592(2.498) M_{\odot}$, which is close to that $M_{\text{b(g),BH}} \sim 2.60(2.51) M_{\odot}$ for Z70 in this work. Regarding S40, the BH formation does not occur in the first 300 ms after bounce, which is consistent with multi-D results by Chan et al. (2018); Pan et al. (2017).

In this study, we have presented results of only the two progenitors. Although one of them leads to the BH formation with a mass of $\sim 2.6 M_{\odot}$, it is a long way to understand the final BH mass (~ 8 to $\sim 30 M_{\odot}$) observed in the GW events (Abbott et al. 2016a,b, 2017). We need to follow a much longer evolution up to the order of $T_{\text{pb}} \sim 10$ s until the entire helium core (at a radius of 10^9 cm) accretes to the BH. To do this, one needs to implement both the apparent horizon finder and some special treatments for neutrinos and fluids within the apparent horizon (e.g., Hawke et al. (2005)). Understanding the dynamics and evolution of the BH-forming massive stars should progress not only with such an update in numerical techniques but also with the advance in binary stellar evolutionary calculations (e.g., Marchant et al. (2016)).

ACKNOWLEDGEMENTS

This research was supported by the European Research Council (ERC; FP7) under ERC Advanced Grant FISH-321263 (TK and FKT), ERC Starting Grant EUROPIUM-677912 (TK), JSPS KAKENHI Grant Number (JP15KK0173 (KK), JP17H05206, JP17K14306, JP15H00789, JP15H01039 (TK), and JP17H01130, JP17H06364 (KK and TT)), and JICFuS as a priority issue to be tackled by using the Post 'K' Computer. Numerical computations were carried out on Cray XC30 at CfCA, NAOJ.

REFERENCES

Abbott B. P., et al., 2016a, *Physical Review Letters*, **116**, 061102
 Abbott B. P., et al., 2016b, *Physical Review Letters*, **116**, 241103
 Abbott B. P., et al., 2016c, *ApJ*, **818**, L22
 Abbott B. P., et al., 2017, *Physical Review Letters*, **118**, 221101
 Baumgarte T. W., Shapiro S. L., 1999, *Phys. Rev. D*, **59**, 024007
 Belczynski K., Dominik M., Bulik T., O'Shaughnessy R., Fryer C., Holz D. E., 2010, *ApJ*, **715**, L138
 Belczynski K., Buonanno A., Cantiello M., Fryer C. L., Holz D. E., Mandel I., Miller M. C., Walczak M., 2014, *ApJ*, **789**, 120
 Blondin J. M., Mezzacappa A., DeMarino C., 2003, *ApJ*, **584**, 971
 Bruenn S. W., 1985, *ApJS*, **58**, 771
 Buras R., Janka H.-T., Rampf M., Kifonidis K., 2006, *A&A*, **457**, 281
 Cardall C. Y., Endeve E., Mezzacappa A., 2013, *Phys. Rev. D*, **88**, 023011
 Cerdá-Durán P., DeBrye N., Aloy M. A., Font J. A., Obergaullinger M., 2013, *ApJ*, **779**, L18
 Chan C., Müller B., Heger A., Pakmor R., Springel V., 2018, *ApJ*, **852**, L19
 Colella P., Woodward P. R., 1984, *Journal of Computational Physics*, **54**, 174
 Fischer T., Whitehouse S. C., Mezzacappa A., Thielemann F.-K., Liebendörfer M., 2009, *A&A*, **499**, 1
 Fryer C. L., Woosley S. E., Hartmann D. H., 1999, *ApJ*, **526**, 152

Hannestad S., Raffelt G., 1998, *ApJ*, **507**, 339
 Hawke I., Löffler F., Nerozzi A., 2005, *Phys. Rev. D*, **71**, 104006
 Heger A., Fryer C. L., Woosley S. E., Langer N., Hartmann D. H., 2003, *ApJ*, **591**, 288
 Hempel M., Fischer T., Schaffner-Bielich J., Liebendörfer M., 2012, *ApJ*, **748**, 70
 Horiuchi S., Sumiyoshi K., Nakamura K., Fischer T., Summa A., Takiwaki T., Janka H.-T., Kotake K., 2018, *MNRAS*, **475**, 1363
 Janka H.-T., Melson T., Summa A., 2016, Annual Review of Nuclear and Particle Science,
 Kinugawa T., Nakano H., Nakamura T., 2016, *Progress of Theoretical and Experimental Physics*, **2016**, 103E01
 Kotake K., Sumiyoshi K., Yamada S., Takiwaki T., Kuroda T., Suwa Y., Nagakura H., 2012, *Progress of Theoretical and Experimental Physics*, **2012**, 010000
 Kuroda T., Kotake K., Takiwaki T., 2012, *ApJ*, **755**, 11
 Kuroda T., Takiwaki T., Kotake K., 2014, *Phys. Rev. D*, **89**, 044011
 Kuroda T., Takiwaki T., Kotake K., 2016, *ApJS*, **222**, 20
 Langer N., 2012, *ARA&A*, **50**, 107
 Lattimer J. M., Swesty F., 1991, *Nuclear Physics A*, **535**, 331
 Lentz E. J., et al., 2015, *ApJ*, **807**, L31
 Liebendörfer M., Messer O. E. B., Mezzacappa A., Bruenn S. W., Cardall C. Y., Thielemann F.-K., 2004, *ApJS*, **150**, 263
 Liebendörfer M., Whitehouse S. C., Fischer T., 2009, *ApJ*, **698**, 1174
 Lunardini C., 2009, *Physical Review Letters*, **102**, 231101
 Marchant P., Langer N., Podsiadlowski P., Tauris T. M., Moriya T. J., 2016, *A&A*, **588**, A50
 Marronetti P., Tichy W., Brüggemann B., González J., Spherhake U., 2008, *Phys. Rev. D*, **77**, 064010
 Mirizzi A., Tamborra I., Janka H.-T., Saviano N., Scholberg K., Bollig R., Hüdepohl L., Chakraborty S., 2016, *Nuovo Cimento Rivista Serie*, **39**, 1
 Müller B., Janka H.-T., Marek A., 2012, *ApJ*, **756**, 84
 O'Connor E., Ott C. D., 2011, *ApJ*, **730**, 70
 Ott C. D., et al., 2011, *Physical Review Letters*, **106**, 161103
 Ott C. D., Roberts L. F., da Silva Schneider A., Fedrow J. M., Haas R., Schnetter E., 2018, *ApJ*, **855**, L3
 Pan K.-C., Liebendörfer M., Couch S. M., Thielemann F.-K., 2017, preprint, ([arXiv:1710.01690](https://arxiv.org/abs/1710.01690))
 Roberts L. F., Ott C. D., Haas R., O'Connor E. P., Diener P., Schnetter E., 2016, *ApJ*, **831**, 98
 Sekiguchi Y.-I., Shibata M., 2005, *Phys. Rev. D*, **71**, 084013
 Shibata M., Nakamura T., 1995, *Phys. Rev. D*, **52**, 5428
 Shibata M., Sekiguchi Y.-I., 2003, *Phys. Rev. D*, **68**, 104020
 Shibata M., Kiuchi K., Sekiguchi Y., Suwa Y., 2011, *Progress of Theoretical Physics*, **125**, 1255
 Sumiyoshi K., Yamada S., Suzuki H., 2007, *ApJ*, **667**, 382
 Takahashi K., Umeda H., Yoshida T., 2014, *ApJ*, **794**, 40
 Thornburg J., 2004, *Classical and Quantum Gravity*, **21**, 743
 Woosley S. E., Heger A., Weaver T. A., 2002, *Reviews of Modern Physics*, **74**, 1015

This paper has been typeset from a $\text{\TeX}/\text{\LaTeX}$ file prepared by the author.